Journal of Materials Chemistry C

PAPER

View Article Online
View Journal | View Issue

Cite this: J. Mater. Chem. C, 2014, 2, 9478

Magnetic graphene oxide nanocomposites: nanoparticles growth mechanism and property analysis

Yiran Wang,[ab] Qingliang He,[abi] Honglin Qu,[ab] Xi Zhang,[ab] Jiang Guo,[ab] Jiahua Zhu,[a] Guanglin Zhao,*[c] Henry A. Colorado,[d] Jingfang Yu,[e] Luyi Sun,[e] Saheel Bhana,[f] Mojammel A. Khan,[g] Xiaohua Huang,[f] David P. Young,[g] Huanwen Wang,[h] Xuefeng Wang,*[h] Suying Wei*[ab] and Zhanhu Guo*[ai]

The growth mechanism of magnetic nanoparticles (NPs) in the presence of graphite oxide (GO) has been investigated by varying the iron precursor dosage and reaction time (product donated as MP/GO). The synthesized magnetic NPs were anchored on the GO sheets due to the abundant oxygen-containing functionalities on the GO sheets such as carboxyl, hydroxyl and epoxy functional groups. The introduced NPs changed the intrinsic functionalities and lattice structure of the basal GO as indicated by FT-IR, Raman and XRD analysis, and this effect was enhanced by increasing the amount of iron precursor. Uniform distribution of NPs within the basal GO sheets and an increased particle size from 19.5 to 25.4, 31.5 and 85.4 nm were observed using scanning electron microscope (SEM) and transmission electron microscope (TEM) when increasing the weight ratio of GO to iron precursor from 10 : 1, to 5 : 1, 1 : 1 and 1 : 5, respectively. An aggregation of NPs was observed when increasing the iron precursor dosage or prolonging the reaction time from 1 to 8 h. Most functionalities were removed and the magnetic NPs were partially converted to iron upon thermal treatment under a reducing condition. The GO and MP/GO nanocomposites reacted for one and two hours (denoted as MP/GO_1-1 h and MP/GO_1-2 h) were converted from insulator to semiconductor after the annealing treatment as annealed GO (A-GO, 8.86 S cm^{-1}), annealed MP/GO_1-1 h (A-MP/GO_1-1 h, 7.48 × 10^{-2} S cm^{-1}) and annealed MP/GO_1-2 h (A-MP/GO_1-2 h, 7.58 × 10^{-2} S cm^{-1}). The saturation magnetization was also enhanced significantly after the annealing treatment, increased from almost 0 to 26.7 and 83.6 emu g^{-1} for A-MP/GO_1-1 h and A-MP/GO_1-2 h, respectively.

Received 24th June 2014
Accepted 11th September 2014

DOI: 10.1039/c4tc01351d

www.rsc.org/MaterialsC

Introduction

Graphene, a two-dimensional sp^2 carbon monolayer in a unique honeycomb-like network, has attracted dramatic attention due to its numerous merits such as extremely large specific surface area (2630 m^2 g^{-1}), high thermal and electrical conductivity (~5000 W m^{-1} K^{-1} and 6000 S cm^{-1}), large Young's modulus (~1.0 TPa) and high optical transmittance (~97.7%).[1–4] Graphene has therefore been widely employed in various applications, such as supercapacitors, batteries, solar cells, photovoltaic cells, gas barriers and other devices.[5–13] Graphene oxide (GO), a graphene-based material, shares merits similar to those of graphene. However, due to the presence of decorated hydroxyl, carboxyl and epoxy functional groups on the basal plane and plane edge,[14] GO is more easily dispersed than graphene, making its synthesis, processing and usage more convenient. In addition, the strong hydrophilicity of GO guarantees that it is a good candidate for many applications, including drug delivery, harmful cell treatment and water purification.[15,16]

In order to enrich the functionalities, graphene and GO are always used to host various nanomaterials due to their large surface area.[17,18] Excellent performances in different areas have been achieved after the incorporation of inorganic NPs. For example, Co_3O_4–anchored graphene nanocomposites that serve as potential electrode materials for supercapacitors exhibit an

[a]Integrated Composites Laboratory (ICL), Dan F Smith Department of Chemical Engineering, Lamar University, Beaumont, TX 77710, USA. E-mail: zhanhu.guo@lamar.edu; zguo10@utk.edu

[b]Department of Chemistry and Biochemistry, Lamar University, Beaumont, TX, 77710 USA. E-mail: suying.wei@lamar.edu

[c]Department of Physics, Southern University, Baton Rouge, LA, 70803 USA. E-mail: guang-lin_zhao@subr.edu

[d]Department of Materials Science and Engineering, University of California Los Angeles, Los Angeles, CA, 90095 USA

[e]Department of Chemical & Biomolecular Engineering, Institute of Materials Science, University of Connecticut, Storrs, CT, 06269 USA

[f]Department of Chemistry, The University of Memphis, Memphis, TN 38152, USA

[g]Department of Physics and Astronomy, Louisiana State University, Baton Rouge, LA, 70803 USA

[h]Department of Chemistry, Key Laboratory of Yangtze River Water Environment, Ministry of Education, Tongji University, Shanghai 200092, China. E-mail: xfwang@tongji.edu.cn

[i]Engineered Multifunctional Composites, LLC, Beaumont, TX 77713, USA

excellent specific capacitance.[19] TiO_2/graphene nanocomposites display a much higher photocatalytic activity and stability for the degradation of benzene in air.[20] Graphene-wrapped Fe_3O_4 nanocomposites exhibit improved reversible capacity and cyclic stability in the lithium ion battery.[21] In addition, graphene based materials also possess the ability to adsorb organic molecules and heavy metal ions, which gives them potential to be adsorbent materials. However, the inconvenient separation and following difficult recycling process have greatly restricted their applications. To overcome this problem, magnetic NPs are usually introduced to improve graphene's efficient adsorption behavior. Previous reports have proven their amazing removal behavior for pollutants, like chromium,[17,22] copper,[23,24] arsenic,[25–27] cadmium,[28] lead,[29] cobalt[30] and organic dye,[30–32] after the introduction of magnetic NPs.

For the synthesis of magnetic graphene or GO-based nanocomposites, GO is commonly used as a template to grip the *in situ* produced magnetic NPs by interacting with the functionalized oxygen-containing groups. A further reduction process is performed to obtain graphene or reduced GO (r-GO) nanocomposites with an enhanced magnetization. Nowadays, the study of graphene-based nanocomposites focuses mainly on their performance and applications; however, the growth mechanism of NPs in the presence of GO is still unclear, and the variations of GO during the NPs depositing and annealing processes have rarely been reported.

In the present work, MP/GO nanocomposites were successfully synthesized in a mild hydrothermal condition using as-fabricated GO and iron nitrate ($Fe(NO)_3$) as raw materials. The growth of NPs on the GO surface was performed by varying the $Fe(NO)_3$ amount and reaction time. The structure, functionality and stability of the as-prepared GO and MP/GO nanocomposites under various conditions were characterized to obtain insight into the inherent growth mechanism. Scanning electron microscopy (SEM), transmission electron microscopy (TEM) and X-ray diffraction (XRD) were used to study the microstructure and crystalline phases of the MP/GO nanocomposites. Fourier transform infrared spectroscopy (FT-IR) and Raman spectroscopy were applied to characterize the functionality and structural evolution of the as-prepared GO and MP/GO nanocomposites. Thermogravimetric analysis (TGA) was also applied to analyze the thermal stability and determine the loading of NPs. The annealing effect on the conductivity and magnetic properties of the as-prepared GO and MP/GO nanocomposites were investigated by a four-probe technique and magnetometer as well.

Materials and methods

Materials

Natural graphite powders were supplied by Bay Carbon Inc, USA. Potassium persulfate ($K_2S_2O_8$, ≥99.0%), phosphorus pentoxide (P_2O_5, ≥98.0%) and potassium permanganate ($KMnO_4$, ≥99.0%) were purchased from Sigma Aldrich. Iron nitrate nonahydrate ($Fe(NO_3)_3 \cdot 9H_2O$, >98.0%), sulfuric acid (H_2SO_4, 93–98%), hydrochloric acid (HCl, 37.5%) and hydrogen peroxide aqueous solution (PERDROGEN® 30% H_2O_2 (w/w)) were purchased from Alfa Aesar. The dialysis membrane (Spectra/Por, molecular weight cutoff (MWCO): 12 000–14 000) was commercially obtained from Spectrum Laboratories, Inc. All the materials were used as received without any further treatment.

Methods

Graphite oxide (GO) was synthesized following a modified Hummers method.[18,33] Specifically, prior to the Hummers synthesis of GO, natural graphite powders first underwent a pre-oxidation process in order to promote the complete oxidation of graphite. In detail, 3.0 g natural graphite powders, 4.0 g $K_2S_2O_8$ and 4.0 g P_2O_5, were weighed and mixed, followed by an addition of 12 mL H_2SO_4, the mixture was then heated to 80 °C and kept for 6 h. After cooling to room temperature, distilled water was used to dilute and wash the products until the rinsed water turned neutral. The pre-oxidized product was dried naturally at room temperature overnight. The dried pre-oxidized intermediate product was dispersed in 120 mL H_2SO_4 at 0 °C, followed by gradual addition of 15.0 g $KMnO_4$, and stirring was continued during this process for the removal of heat while the temperature was controlled below 20 °C. The mixture was transferred to a water bath and kept at 35 °C for 2 h with magnetic stirring to complete the oxidation process. Finally, 250 mL distilled water was added and 15 min later, another 700 mL distilled water and 20 mL H_2O_2 solution were added in sequence to terminate the oxidation reaction. The solution turned from blackish purple to bright yellow and was filtered and washed with 1 L HCl aqueous solution (1 : 9 v/v) to remove metal ions. The obtained GO slurry was re-dispersed with certain amount of distilled water to form a 1.5 wt% diluted suspension, which was further subjected to a dialysis process within a dialysis membrane package to completely remove the residual metal ions and acid. The final concentration of the as-synthesized GO aqueous solution was determined to be 1.17 wt% by measuring the weight difference before and after drying at 60 °C overnight.

The MP/GO nanocomposites were synthesized using a GO suspension and $Fe(NO)_3$ as precursors. Specifically, 17.1 g GO aqueous solution (0.2 g GO) was dispersed in 50 mL distilled water and subjected to a one-hour ultrasonication to achieve the uniform dispersion of individual GO sheets. The suspension was then placed in water bath and maintained at 70 °C with 300 rpm magnetic stirring, 50 mL $Fe(NO)_3$ aqueous solution containing different precursor amounts ($GO : Fe(NO)_3 = 10 : 1$, 5 : 1, 1 : 1, and 1 : 5, products labeled as MP/GO_{10}, MP/GO_5, MP/GO_1 and $MP/GO_{0.2}$, respectively) was added dropwise to start the reaction. The beaker was removed from the water bath after 8 h and cooled down to room temperature. The synthesized MP/GO nanocomposites were filtered and washed with distilled water until the rinsed water turned neutral. 17.1 g GO aqueous solution without the addition of $Fe(NO)_3$ was also employed as a control experiment, and this solution was named as GO, and all the products were dried at 60 °C overnight. $GO : Fe(NO)_3 = 1 : 1$ was selected to investigate the reaction time effect by applying different reaction time as 1 h or 2 h (products labeled as MP/GO_1-1 h and MP/GO_1-2 h). The annealing process was

performed by heating GO, MP/GO_1-1 h, and MP/GO_1-2 h up to 800 °C for 2 h under a H_2 atmosphere balanced with 95% argon (products designated as A-GO, A-MP/GO_1-1 h and A-MP/GO_1-2 h, respectively). The detailed synthesis parameters for the specific samples are summarized in Table 1.

Characterizations

Fourier transform infrared spectroscopy (FT-IR, Bruker Inc. Vector 22, coupled with an ATR accessory) was used to characterize the structure of the synthesized nanocomposites over the range of 500 to 4000 cm^{-1} with a resolution of 4 cm^{-1}.

The morphology of the synthesized nanocomposites was characterized using scanning electron microscopy (SEM, Hitachi S-3400) and transmission electron microscopy (TEM, FEI TECNI G2 F20) with a field emission gun, operated at an accelerating voltage of 200 kV. The TEM samples were extracted from the hot solution of GO nanocomposites at the end of each synthesis process, after dilution with about 10 times of DI water, and one droplet was dropped on a 400 mesh carbon-coated copper grid. The NPs size were measured using Nano Measure software for over 200 NPs.

The thermal stability of the synthesized nanocomposites was studied using a thermal gravimetric analysis (TGA Q-500, TA Instruments) in air and nitrogen atmosphere, respectively, with a flow rate of 60 mL min^{-1} and a heating rate of 10 °C min^{-1}.

X-ray diffraction (XRD) analysis was carried out using a Bruker AXS D8 Discover diffractometer operating with a Cu-K_α radiation source. The XRD patterns were recorded at 2θ from 5° to 80°.

The Raman signals were collected with a ProRaman-L porter Raman spectrometer (Enwave Optronics, Irvine, CA) and recorded from 1100 to 1800 cm^{-1}. The focus of the laser was adjusted to obtain maximum signal, which was detected with a CCD camera cooled down to −60 °C. The excitation wavelength was 785 nm and the power was 50 mW with an acquisition time of 5 s. A baseline correction using multi-segment polynomial fitting (provided by EnWave) was utilized to subtract the background.

The electrical conductivity of each sample was measured by a four-probe technique (C4S 4-Point Probe Head, Cascade Microtech, the tips were made of tungsten carbide).

Table 1 Synthesis parameters for different nanocomposites

Sample ID	Precursor ratios	Reaction time (h)	Annealing
GO	GO : Fe = 10 : 0	—	No
MP/GO_{10}	GO : Fe = 10 : 1	8	No
MP/GO_5	GO : Fe = 5 : 1	8	No
MP/GO_1	GO : Fe = 1 : 1	8	No
MP/$GO_{0.2}$	GO : Fe = 1 : 5	8	No
MP/GO_1-1 h	GO : Fe = 1 : 1	1	No
MP/GO_1-2 h	GO : Fe = 1 : 1	2	No
A-GO	GO : Fe = 10 : 0	—	Yes
A-MP/GO_1-1 h	GO : Fe = 1 : 1	1	Yes
A-MP/GO_1-2 h	GO : Fe = 1 : 1	2	Yes

The magnetic property of the samples at room temperature was recorded in a 9T physical properties measurement system (PPMS) by Quantum Design.

Results and discussion

Microstructure investigation

The morphologies of MP/GO_{10}, MP/GO_5, MP/GO_1 and MP/$GO_{0.2}$ were characterized by SEM, as shown in Fig. 1(a)–(d). All the NPs are observed to be successfully synthesized and anchored on the GO surface. For MP/GO_{10} with ultra-low NP loading, seen in Fig. 1(a), the GO surface still maintained smooth morphology attached by a few small NPs, and the size of decorated NPs was estimated as 19.5 nm. More NPs became anchored on the GO surface with increasing the ion precursor amount, and the particle size increased to 25.4, 31.5 and 85.4 nm for MP/GO_5, MP/GO_1 and MP/$GO_{0.2}$, respectively (Fig. 1(b–d)). The increased particle size clearly indicates that increasing the dosage of $Fe(NO)_3$ can directly result in the increase of NPs size. In addition, it is clearly seen that the GO surface became rougher when increasing the NPs loading, which is also observed in the CdS/rGO nanocomposites;[34] moreover, the wrinkled structure probably came from the restacking process, as the mobility of GO sheets was largely restricted by the fixed NPs.[35]

Fig. 2(a)–(e) show the FT-IR spectra of the as-prepared GO, MP/GO_{10}, MP/GO_5, MP/GO_1 and MP/$GO_{0.2}$, respectively. For the as-prepared GO (Fig. 2(a)), two absorbance peaks at 1623 and 1726 cm^{-1} are clearly observed, which are attributed to the stretching vibrations of aromatic C=C and C=O groups, respectively.[18,36,37] The peaks at 1223 and 1056 cm^{-1} are assigned to the epoxy C–O and alkoxy C–O groups located at the edges of the GO sheets.[36,38–40] The peak at 1379 cm^{-1} arises from the bending vibration of hydroxyl groups attached to the aromatic carbon backbone.[41–43] The peak at 969 cm^{-1} belongs to peroxide group vibration.[44] Because it has been confirmed that no peaks are observed in the FT-IR spectra of graphite,[45,46] all these oxygen-containing functional groups were generated

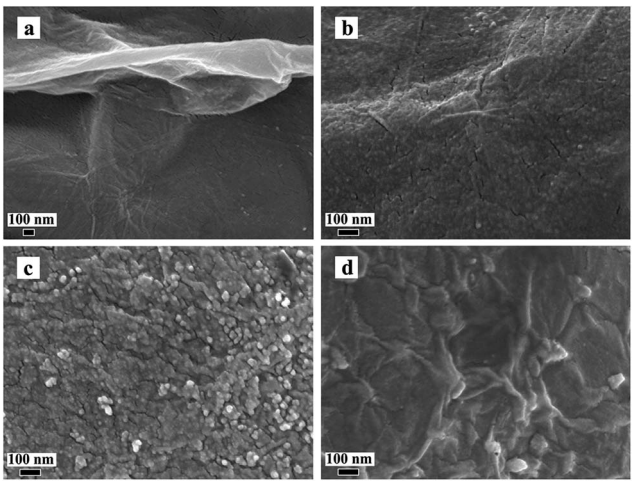

Fig. 1 SEM images of (a) MP/GO_{10}, (b) MP/GO_5, (c) MP/GO_1 and (d) MP/$GO_{0.2}$.

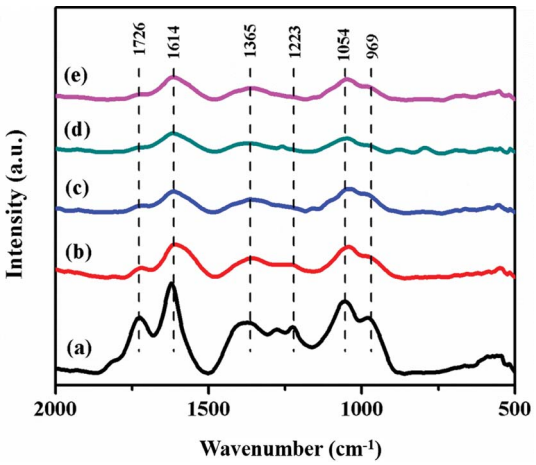

Fig. 2 FT-IR spectra of (a) as-prepared GO, (b) MR/GO_{10}, (c) MR/GO_5, (d) MR/GO_1 and (e) MR/$GO_{0.2}$.

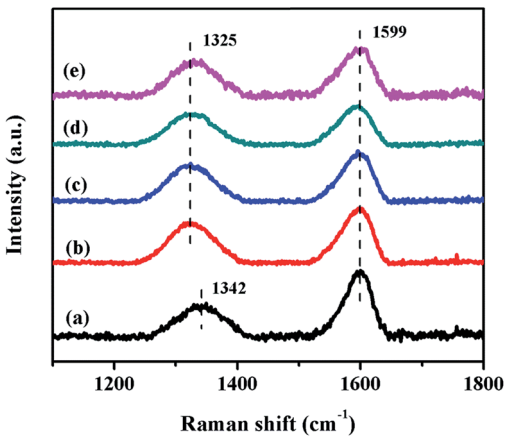

Fig. 3 Raman spectra of (a) as-prepared GO, (b) MP/GO_{10}, (c) MP/GO_5, (d) MP/GO_1 and (e) MP/$GO_{0.2}$.

during the strong oxidation process, which indicates the successful modification of graphene through a modified Hummers method. For MP/GO_{10}, MP/GO_5, MP/GO_1 and MP/$GO_{0.2}$, Fig. 2(b)–(d), similar spectrum patterns as that of GO are observed, revealing that the functional groups have not been destroyed after the deposition of NPs. However, it is clearly seen that the peak intensity and position of the functional groups have been changed, and the intensity for all peaks becomes much weaker with increase in the loading of NPs, especially for the epoxy C–O group at 1223 cm^{-1}, which almost disappears in MP/GO_5, MP/GO_1 and MP/$GO_{0.2}$ due to the removal of the corresponding functional groups during the deposition of NPs.[47] In addition, the peaks at 1623, 1379 and 1056 cm^{-1} exhibit downshifts to lower wavenumbers at 1609, 1352 and 1045 cm^{-1}, respectively, which is probably correlated with the presence of hydrogen bonding between the functional groups and the as-synthesized NPs.[48,49] Similar results have also been reported in iron oxide/GO nanocomposites synthesized through a hydrothermal method.[50] Finally, the affected basal structure of GO is mainly accountable for the position change of the C=C bond due to the decoration of the as-synthesized NPs.

The Raman spectrum is a prominent tool used to characterize the crystalline structure of carbon materials, especially for those possessing conjugated C=C bonds, due to its strong response to the specific electronic property.[51–53] Fig. 3 shows the Raman spectra of the as-prepared GO, MP/GO_{10}, MP/GO_5, MP/GO_1 and MP/$GO_{0.2}$. Typically, the Raman spectrum of graphene based materials shows two feature peaks: a G band and a D band. The G band is attributed to the E_{2g} phonon mode of in-plane sp^2 carbon atoms, and the D band is induced by the interruption of regular hexagonal network structure, including in-plane defects, edge defects and dangling bonds.[54,55] For the as-prepared GO (Fig. 3(a)), two characteristic peaks are clearly observed as 1599 cm^{-1} for the G band and 1342 cm^{-1} for the D band. The presence of the D band indicates that the original lattice structure of graphite was disrupted by the introduced functional groups.[52,56,57] In addition, it is clearly seen that all D bands of the four MP/GO nanocomposites shift to a lower wavenumber (1325 cm^{-1}) compared with that of the as-prepared GO, which is consistent with $NiFe_2O_4$/GO and polyethylene glycol/GO nanocomposites.[47,58] This phenomenon is probably due to the NPs anchored to the GO surface that behave like defects and largely damage the intrinsic bonds and symmetry.[55,59] The intensity ratio of D band and G band (I_D/I_G) determines the structure of graphene-based materials, and a higher I_D/I_G value indicates more defects and disordered structure on the GO surface.[14,60] A monotonous increase of I_D/I_G value was obtained, as summarized in Table 2, showing a dramatic increase of the I_D/I_G value from the as-prepared GO (0.47) to 0.72, 0.74, 0.78 and 0.76 for MP/GO_{10}, MP/GO_5, MP/GO_1 and MP/$GO_{0.2}$; moreover, these increases indicate that increasing the number of anchored NPs on the GO surface can cause more structural defects. Finally, the in-plane crystalline size (L_a) is also calculated using an empirical formula eqn (1), and the calculated values are summarized in Table 2.[61]

$$L_a = \frac{560}{E_\lambda^4}\left(\frac{I_D}{I_G}\right)^{-1} \quad (1)$$

where E_λ is the excitation laser energy in eV used in the Raman measurement. It is obtained from Table 2, which shows that all the GO nanocomposites exhibit smaller L_a values compared with that of the as-prepared GO due to the affected basal structure by the anchored NPs, consistent with the downshift of the C=C peak in FT-IR spectra. In addition, the presence of NPs has another effect, *i.e.*, it prevents the agglomeration of

Table 2 Summary of the I_D/I_G and L_a values of synthesized MP/GO nanocomposites

Sample ID	I_D/I_G	L_a (nm)
GO	0.47	190.9
MP/GO_{10}	0.72	124.8
MP/GO_5	0.74	121.8
MP/GO_1	0.78	115.3
MP/$GO_{0.2}$	0.76	118.8

substrate sheets, thus contributing to the decreased L_a value. Furthermore, a monotonous decrease in L_a values is observed for MP/GO_{10}, MP/GO_5, MP/GO_1 and MP/$GO_{0.2}$, indicating an enhanced effect with increasing the NPs loading. However, for MP/$GO_{0.2}$, a slight L_a increase of GO is observed due to the full usage of the constant GO defects at the same GO amount, which is also consistent with the approached constant I_D/I_G value in the synthesized MP/GO nanocomposites.

TGA is the powerful technique employed to investigate the thermal stability and determine the loading of the synthesized MP/GO nanocomposites. Fig. 4(A) and (B) shows the TGA curves of GO, $Fe(NO_3)_3 \cdot 9H_2O$ and MP/GO nanocomposites in air and in a nitrogen atmosphere, respectively, as (a) as-prepared GO, (b) MP/GO_{10}, (c) MP/GO_5, (d) MP/GO_1, (e) MP/$GO_{0.2}$ and (f) $Fe(NO)_3 \cdot 9H_2O$. For TGA curves in air atmosphere (Fig. 4(A)), all these TGA curves experience a typical thermal decomposition process in air atmosphere, and it is clearly seen that $Fe(NO_3)_3 \cdot 9H_2O$ exhibits the poorest thermal stability as it was decomposed completely and eventually was converted to Fe_2O_3 around 350 °C.[62] For the as-prepared GO, a weight loss of 10% below 150 °C was assigned to the evaporation of physically absorbed water.[36] As the temperature rises, the observed significant weight loss at around 200 °C is due to the removal of labile oxygen-containing functional groups. The following slow weight loss is due to the decomposition of stable oxygen functionalities. Finally, GO gets burned out at around 690 °C.[18] For MP/GO_{10}, MP/GO_5, MP/GO_1 and MP/$GO_{0.2}$, similar thermal decomposition patterns to that of the as-prepared GO are observed; however, the final residual weight percentages (F.W.) and the decomposition temperatures vary with the iron precursor amounts. It is clearly seen from Table 3 that higher iron salt dosages result in higher F.W. values, which is also consistent with the SEM analysis. However, even though the iron precursor amount of MP/$GO_{0.2}$ is 4 times more than that of MP/GO_1 with the same GO base, the final residues of these two are almost the same (58.7% for MP/$GO_{0.2}$ and 56.5% for MP/GO_1), demonstrating that the NPs have occupied almost all the defects on the GO surface and reached the saturation status of GO. Moreover, it is clearly seen that the decomposition temperature of the functionalized groups and the final stable temperature also change with varying the $Fe(NO)_3$ amount. The $t1$, $t2$ and $t3$ values represent the on-set removal temperature of liable functional groups,[18] the maximum oxidation temperature of the residual carbon and the beginning temperature of the final stable status, respectively. The $t2$ and $t3$ values of all the synthesized MP/GO nanocomposites are observed to be lower than that of GO, indicating that the anchored NPs can accelerate the heat transfer and the oxidation of carbon. However, an increased $t1$ value is observed for MP/GO nanocomposites compared with that of the as-prepare GO, suggesting that the removal of labile functional groups is hindered by the occupation of functionalized groups by the NPs. Finally, it is clearly obtained from Table 3 that the $t2$ and $t3$ values decrease when increasing the NPs loading, which can be explained by the increased NPs loadings inevitably decreasing the carbon amount within the nanocomposites, thus leading to the earlier burn off of the carbon materials.

Table 3 Thermal stability parameters of GO and MP/GO nanocomposites

Sample ID	F. W. (%)	$t1$ (°C)	$t2$ (°C)	$t3$ (°C)
GO	0	167.71	645.40	687.75
MP/GO_{10}	9.4	184.85	411.72	463.90
MP/GO_5	18.3	187.12	382.98	438.19
MP/GO_1	56.5	195.61	348.20	435.16
MP/$GO_{0.2}$	58.7	196.51	345.17	417.77

Fig. 4(B) shows the thermal stability of the corresponding nanocomposites under a nitrogen atmosphere. As the temperature goes below 200 °C, all the decomposition patterns of the as-synthesized nanocomposites are close to those under an air condition, indicating the removal of absorbed water and labile oxygen-containing functional groups on the GO surface. However, as temperature increases above 300 °C, GO undergoes a slow and smooth weight loss, which is assigned to the thermal decomposition of stable oxygen functionalities.[63] Because carbon material cannot be oxidized or burned under an inert condition, the residual weight percentages are not stabilized

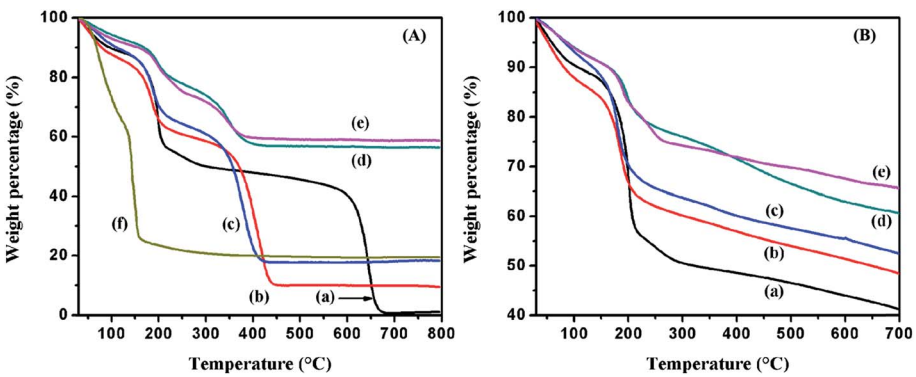

Fig. 4 TGA curves in (A) air atmosphere and (B) nitrogen atmosphere for (a) as-prepared GO, (b) MP/GO_{10}, (c) MP/GO_5, (d) MP/GO_1, (e) MP/$GO_{0.2}$ and (f) precursor $Fe(NO_3)_3 \cdot 9H_2O$.

and continue to decrease throughout the entire temperature range, as indicated by all the decomposition curves.

The lattice structure of the as-prepared GO and the structural variation after the introduction of NPs were studied by XRD. Fig. 5 shows the XRD patterns of the as-prepared GO, MP/GO_{10}, MP/GO_5, MP/GO_1 and $MP/GO_{0.2}$. For the as-prepared GO (Fig. 5(A)), the strong diffraction peak at 11.64° was used to calculate the interlayer distance (d) using Bragg's law, *i.e.* eqn (2).[64]

$$n\lambda = 2d\cdot\sin\theta \quad (2)$$

where n is chosen as 1, λ is the wavelength of Cu-K_α radiation as 1.5406 Å and θ is the Bragg angle. The d of the as-synthesized GO is calculated to be 7.6 Å, which is very close to the published results for GO[44,65] and much larger than that of graphite measured in our previous work, 3.4 Å.[18] The severe oxidation during GO synthesis process breaks the original lattice structure of graphite and expands the interlayer space of graphite, thus leading to an increased d value. Fig. 5(B) shows the XRD patterns of (a) MP/GO_{10}, (b) MP/GO_5, (c) MP/GO_1 and (d) $MP/GO_{0.2}$. For MP/GO_{10} and MP/GO_5, strong diffraction peaks similar to those of the as-prepared GO around 12° are observed, and the corresponding d values are calculated to be 7.2 and 7.5 Å, respectively, indicating a negligible effect of the small amount and poor crystallinity of NPs on GO. However, the increased NPs loadings can not only damage the original lattice structure of the GO substrate but also largely depress the carbon signal; moreover, the peak intensity of GO becomes negligible, whereas the peaks of magnetic NPs become dominant as well, as indicated by MP/GO_1 and (d) $MP/GO_{0.2}$. Several diffraction peaks (020), (110), (120), (130), (021), (111), (221), (151) and (002) corresponding to pure orthorhombic a-FeOOH (JCPDS 29-713) become intensified with increasing the NPs loading, indicating that the formed NPs exist as a-FeOOH.[66] However, the low intensity of FeOOH peaks clearly indicates the poor crystallinity. In addition, the average grain size (L) is evaluated through Debye–Scherrer equation, *i.e.* eqn (3).[67,68]

$$L = \frac{K\lambda}{\beta(2\theta)\cos\theta} \quad (3)$$

where K is the shape factor depending on the Miller index of the reflecting plane and the shape of the crystal, which is usually assigned as 0.9 for an uncertain shape; λ is the X-ray wavelength as 1.5406 Å; θ is the diffraction angle and $\beta(2\theta)$ is the full width at half-maximum (FWHM). The grain sizes of the as-prepared GO, MP/GO_{10} and MP/GO_5 were calculated to be 8.91, 2.97 and 3.19 nm using the peaks located around 11.6°. The reduced grain size is probably due to the anchored NPs, which cause the separation of nanosheets.

As concluded from the TGA result, the as-prepared GO almost reaches a saturation state in MP/GO_1 nanocomposites. In this case, precursor ratio as $Fe(NO_3)_3$ to GO as 1 : 1 was chosen to investigate the reaction time effect (1 h and 2 h, products labeled as MP/GO_1-1 h and MP/GO_1-2 h). The morphology and crystallization of the NPs were characterized by transmission electron microscopy (TEM) and selected area electron diffraction (SAED). Fig. 6 shows the TEM images (a–c) and SAED patterns (d–f) of MP/GO_1-1 h, MP/GO_1-2 h and MP/GO_1, respectively, and the bottom insets of TEM images are the corresponding high-resolution TEM (HRTEM) with a marked lattice fringe of magnetic NPs. For MP/GO_1-1 h (Fig. 6(a)), the NPs are clearly seen to grow on the GO sheet with ultra-fine particle size (2.98 nm). However, the wide coverage of the GO with self-linked ultra-fine NPs clearly demonstrates that the reaction is proceeding. For MP/GO_1-2 h (Fig. 6(b)), the NPs are observed to continue grow and aggregate into bigger ones with an average size of 14.44 nm. For MP/GO_1, the NPs formed with 8-hour reaction time are around 29.96 nm with a serious aggregation, as shown in Fig. 6(c), which is also consistent with the measured size from the SEM image. The growth mechanism of magnetic NPs is summarized by the following process: the as-synthesized magnetic molecules are first anchored on the GO surface by interacting with the oxygen containing groups, and then the growth proceeds as more molecules are deposited around the nuclei and gradually aggregate into larger NPs with increasing the reaction time. Lattice fringes at 3.37, 2.69, and 2.45 Å belonging to the (1 2 0), (1 0 0), and (1 1 1) planes of α-FeOOH are clearly observed in the bottom inset of the HRTEM images, indicating the successful synthesis of α-FeOOH/GO nanocomposites. For the corresponding SAED patterns (Fig. 6(d)–(f)), the assigned (1 3 0), (1 1 1), (1 4 0), (2 2 1), (1 5 1)

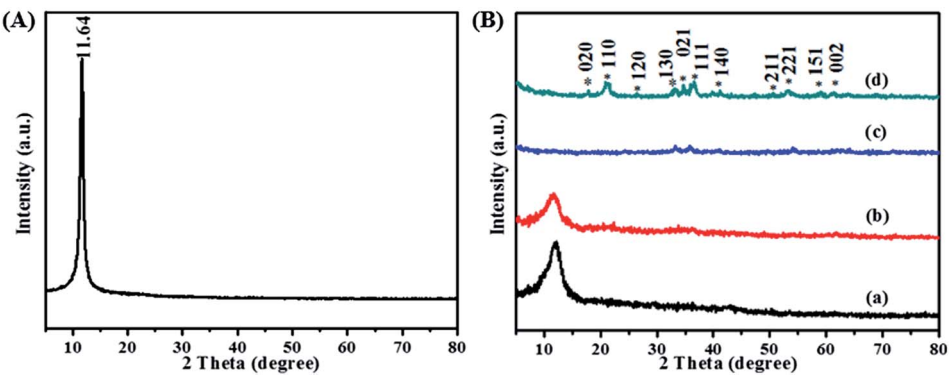

Fig. 5 X-ray diffraction patterns of (A) as-prepared GO and (B) (a) MP/GO_{10}, (b) MP/GO_5, (c) MP/GO_1, (d) $MP/GO_{0.2}$.

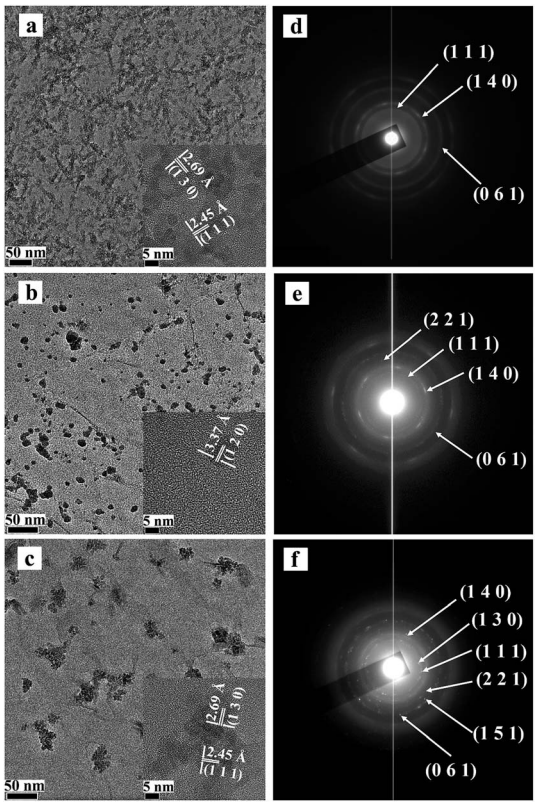

Fig. 6 TEM (a–c) images and corresponding SAED pattern (d–f) of MP/GO_1-1 h, MP/GO_1-2 h, and MP/GO_1. Bottom insets of TEM images are the HRTEM with clear lattice fringe.

and (0 6 1) diffraction planes correspond to α-FeOOH, which is also consistent with the XRD result and HRTEM analysis.[69] Even though these three SAED patterns point to the same material, α-FeOOH, the SAED patterns exhibit different rings varying with the reaction time, obtuse and thick diffraction rings for MP/GO_1-1 h, and the increasing clearer and sharper rings for MP/GO_1-2 h and MP/GO_1 indicate an increase of particle size. In addition, more diffraction planes are observed with increasing the reaction time, *i.e.*, (2 2 1) for Fig. 6(e) and (1 3 0) as well as (1 5 1) for Fig. 6(f), indicating a better growth of crystalline structure with longer reaction time. Therefore, the selection of reaction time is critical for determining the quality of synthesized nanocomposites, as increase in the reaction time could favor the crystal structure but limit the growth of smaller crystal NPs.

Fig. 7(a) and (b) shows the SEM images of A-MP/GO_1-1 h and A-MP/GO_1-2 h, respectively. Both wrinkled structures of the reduced GO substrate are observed, indicating that the GO structure has not been destroyed during the annealing process. However, a much rougher morphology is observed in A-MP/GO_1-2 h than that of A-MP/GO_1-1 h because more NPs are anchored on the GO surface after a longer reaction time. Finally, obvious particle increases are observed for A-MP/GO_1-1 h and A-MP/GO_1-2 h (28.18 and 56.73 nm) in comparison with MP/GO_1-1 h and MP/GO_1-2 h (2.98 and 14.44 nm), indicating further aggregations during the annealing process.

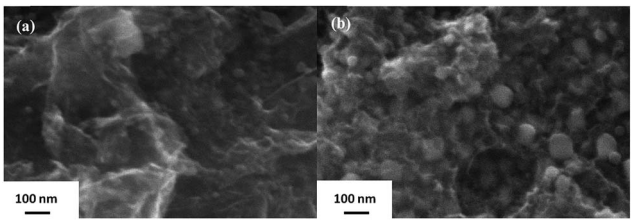

Fig. 7 SEM images of (a) A-MP/GO_1-1 h and (b) A-MP/GO_1-2 h.

Fig. 8(a) and (b) shows the TGA curves of A-MP/GO_1-1 h and A-MP/GO_1-2 h in an air atmosphere. Both slight weight increases are observed that start around 150 °C and stop at 460 °C for A-MP/GO_1-1 h and 380 °C for A-MP/GO_1-2 h. Since FeOOH can be converted to Fe_2O_3, which will be further partially reduced to Fe during the 800 °C reducing heat treatment, the slight weight increase is probably attributable to the oxidation of reduced Fe_2O_3. The final residuals as 67.4 and 70 wt% are obtained for A-MP/GO_1-1 h and A-MP/GO_1-2 h, respectively, which again confirms higher NPs loading in MP/GO_1-2 h than that of MP/GO_1-1 h. In addition, it is clearly seen that the A-MP/GO_1-2 h reaches the final residual weight at a lower temperature, and its maximum weight percent (102.5%) is also lower than that of A-MP/GO_1-1 h (107.1%). This phenomenon is explained by combining the two trends of thermal decomposition of carbon and oxidation of reduced Fe_2O_3, which produce opposing effects on the weight percentage. Because more Fe exists within A-MP/GO_1-2 h, the relatively smaller amount of carbon is decomposed more easily and earlier compared with that of A-MP/GO_1-1 h, thus causing a lower oxidation peak value and lower final stable temperature.

After undergoing the annealing treatment under reducing atmosphere, XRD and Raman spectroscopy were re-employed to characterize the structure conversion of the NPs and GO substrate. Fig. 9(a) and (b) shows the XRD of A-MP/GO_1-1 h and A-MP/GO_1-2 h, and new peaks belonging to (110), (113), (024), (214) and (300) facets of α-Fe_2O_3 (JCPDS 89-596) are clearly seen, indicating the conversion from α-FeOOH to α-Fe_2O_3 during the

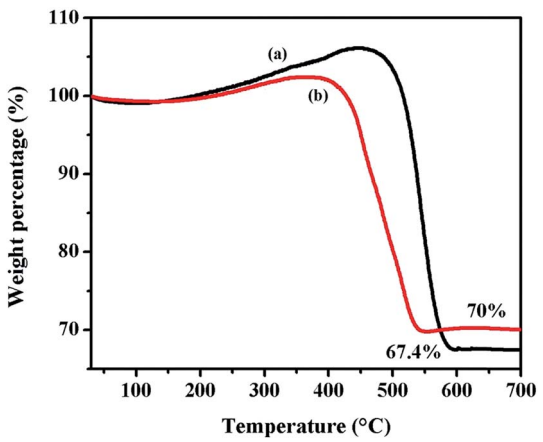

Fig. 8 TGA curves of (a) A-MP/GO_1-1 h and (b) A-MP/GO_1-2 h in air atmosphere.

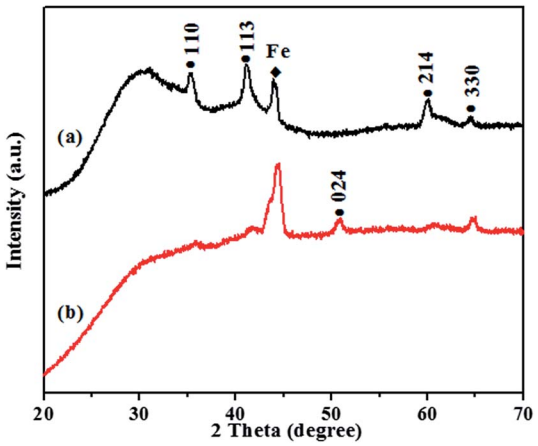

Fig. 9 XRD patterns of (a) A-MP/GO_1-1 h and (b) A-MP/GO_1-2 h.

heat treatment.[70] In addition, the presence of a peak located around 44° corresponds to the zero-valence iron (α-Fe) crystalline phases,[71] indicating a reduction of α-Fe_2O_3 during the annealing process. However, the reduction of α-Fe_2O_3 is incomplete, as confirmed by the presence of α-Fe_2O_3 peaks. A significant increase of α-Fe peak intensity and largely decreased α-Fe_2O_3 peak intensities are observed in A-MP/GO_1-2 h due to the higher NPs loading, which leads to a more thorough reduction process compared with that of A-MP/GO_1-1 h.

Fig. 10(a)–(f) depict the Raman spectra of the as-prepared GO, A-GO, MP/GO_1-1 h, MP/GO_1-2 h, A-MP/GO_1-1 h and A-MP/GO_1-2 h, respectively. For GO and A-GO, Fig. 10(a) and (b), the G band is observed to downshift from 1599 to 1589 cm^{-1} due to the recovery of the defects in hexagonal network structure, as the introduced functional groups are removed during the reduction process.[54] For the Raman spectra of MP/GO_1-1 h, MP/GO_1-2 h, A-MP/GO_1-1 h and A-MP/GO_1-2 h (Fig. 10(c)–(f)), similar downshifts of the D band after annealing treatment are observed due to the recovery of the GO network. In addition, the I_D/I_G values are calculated for all these six samples and are summarized in Table 4. Both MP/GO_1-1 h and MP/GO_1-2 h obtain higher I_D/I_G values than that of the as-prepared GO due to the anchored NPs on the GO surface, which is also consistent with the increased I_D/I_G values when increasing the iron precursor amount. For A-MP/GO_1-1 h and A-MP/GO_1-2 h, increased I_D/I_G values after the annealing treatment are obtained due to the increased defects caused by the destruction of carbon structure. The calculated L_a values for all samples are also listed in Table 4, and all the L_a values are observed to decrease after the annealing treatment, which is probably attributable to the broken graphitic domains and the increased quantity of sp^2 clusters.[72]

The variation of electrical conductivity after the annealing treatment is measured through a four-probe technique, and the obtained voltage-current (*V–I*) curves of A-GO, A-MP/GO_1-1 h, and A-MP/GO_1-2 h are shown in Fig. 11. For the as-prepared GO, MP/GO_1-1 h and MP/GO_1-2 h, the resistance of the three are all in mega-ohm order and considered as insulators. However, after the annealing treatment, it is clearly seen that the current increases linearly with the voltage for A-GO, A-MP/GO_1-1 h, and A-MP/GO_1-2 h within −1.0 to 1.0 V, which indicates constant conductivities, calculated to be 8.86, 7.48 × 10^{-2}, and 7.58 × 10^{-2} S cm^{-1}, respectively. The transition from insulator to semiconductor is probably due to the removal of functionalized oxygen-containing groups and reparation of the basal graphene substrate in the reducing atmosphere, which contributes to the increase in electrical conductivity.[72] However, the conductivity of the reduced GO is still lower than other previously reported results (58.8 and 309 S cm^{-1}) due to the incomplete reduction.[73,74] For A-MP/GO_1-1 h, and A-MP/GO_1-2 h, the same reason is accountable for the enhanced conductivity; however, the enhanced conductivity is still two orders lower than that of A-

Table 4 The summary of I_D/I_G and L_a values for annealed nanocomposites

Sample ID	I_D/I_G	L_a (nm)
GO	0.47	190.9
A-GO	0.79	114.0
MP/GO_1-1 h	0.65	138.0
A-MP/GO_1-1 h	0.80	112.9
MP/GO_1-2 h	0.77	116.0
A-MP/GO_1-2 h	0.79	114.2

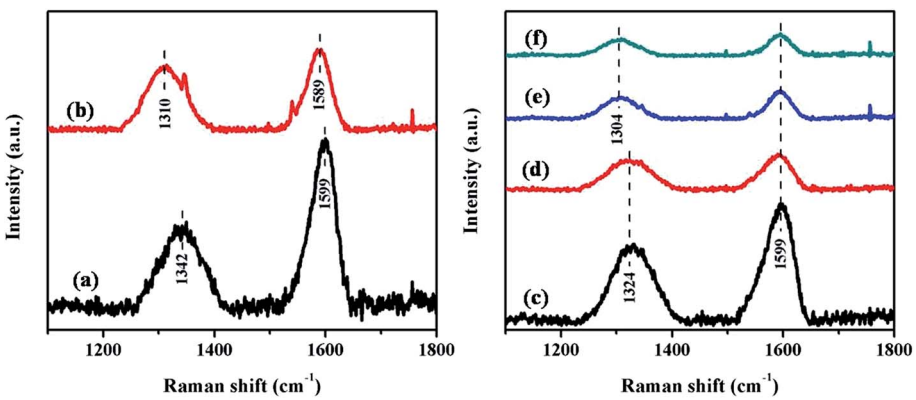

Fig. 10 Raman spectra of (a) GO, (b) A-GO, (c) MP/GO_1-1 h, (d) MP/GO_1-2 h, (e) A-MP/GO_1-1 h and (f) A-MP/GO_1-2 h.

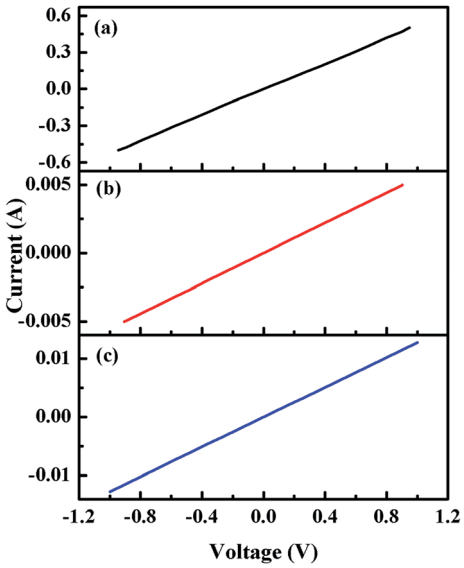

Fig. 11 *V–I* curve of (a) A-GO, (b) A-MP/GO_1-1 h and (c) A-MP/GO_1-2 h.

GO because the anchored NPs that behave as defects can largely affect the basal plane and impede the reparation of their located area, thus lowering the conductivity.

The variation of the magnetic property after the annealing process is also characterized, and the hysteresis loops are shown in Fig. 12 as (a) A-MP/GO_1-1 h and (b) A-MP/GO_1-2 h. The hysteresis loops of MP/GO_1-1 h and MP/GO_1-2 h are also shown in the bottom of Fig. 12, and they exhibit an extremely weak magnetic property due to the low saturation magnetization of FeOOH.[75] However, it is clearly seen from Fig. 12 that the magnetic behaviors have improved significantly as the M_s values increase to 26.7 and 83.6 emu g^{-1} for A-MP/GO_1-1 h and A-MP/GO_1-2 h due to the reduction of α-Fe_2O_3 to Fe (M_s, 218 emu g^{-1}).[76] Since the NPs loading in MP/GO_1-2 h is higher than that of MP/GO_1-1 h, it is reasonable that more α-Fe_2O_3 can be reduced in MP/GO_1-2 h, thus contributing to a higher M_s value than that of A-MP/GO_1-1 h. The top inset of Fig. 12 is a magnification of hysteresis loops, the coercivities (coercive force, H_c) are observed to be 51 Oe for A-MP/GO_1-1 h and 85 Oe for A-MP/GO_1-2 h. In addition, the corresponding remnant magnetizations (M_r, the residue magnetization after the applied field was reduced to zero) were also obtained as 1.5 and 3.3 emu g^{-1}, which indicate the ferromagnetically soft property of the reduced materials.

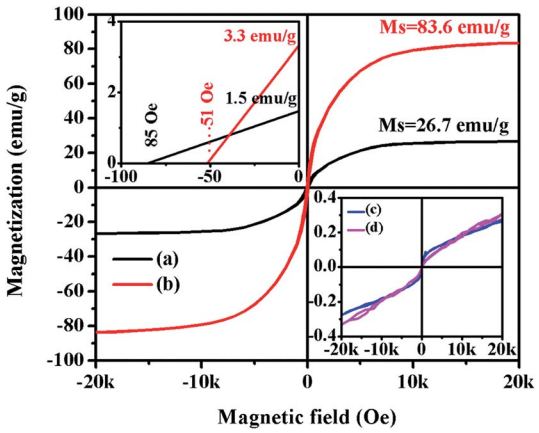

Fig. 12 Room temperature hysteresis loops of (a) A-MP/GO_1-1 h and (b) A-MP/GO_1-2 h. The top inset shows the enlarged partial curve around the origin, and the bottom inset shows the hysteresis loop of (c) MP/GO_1-1 h and (d) MP/GO_1-2 h.

Conclusions

The synthesis mechanism of MP/GO nanocomposites has been systematically investigated by employing different $Fe(NO)_3$ precursor amounts and applying different reaction time. GO with abundant oxygen-containing functional groups serve as a template that can grip the *in situ* formed magnetic NPs, thus leading to a uniform distribution. The anchored NPs can largely affect the lattice structure and functionalities of GO, and this effect is significantly enhanced with increasing $Fe(NO_3)_3$ dosage and finally lead to a full usage of GO defects. On the other hand, varying reaction time can directly affect the growth NPs, as the formation of magnetic NPs follows a growth order as follows: interacting with oxygen containing groups on GO surface; continuing deposition around the nuclei; and aggregation into larger NPs when further increasing the reaction time. After thermal treatment under reducing environment, the electrical conductivity is improved significantly due to the removal of functional groups. However, the presence of NPs mainly accounts for the poor conductivity of A-MP/GO_1-1 h and A-MP/GO_1-2 h compared with that of A-GO, as the NPs act as defects that can greatly impede the reparation of original network. With the production of iron after the annealing treatment in a reducing atmosphere, the magnetic properties of A-MP/GO_1-1 h and A-MP/GO_1-2 h were also improved significantly and exhibited ferromagnetic soft behavior.

Acknowledgements

This work is partially supported by the NSF – National Science Foundation – Chemical and Biological Separation under the EAGER program (CBET 11-37441), and the Air Force Office of Scientific Research (FA9550-09-1-0367 and FA9550-11-1-0330). We acknowledge the support from the National Science Foundation – Nanoscale Interdisciplinary Research Team and Materials Processing and Manufacturing (CMMI 10-30755) to obtain the DSC and TGA. D. P. Young acknowledges support from the NSF under Grant no. DMR 13-06392. S. Wei acknowledges support from the Welch Foundation (V-0004).

References

1 Y. Zhu, S. Murali, W. Cai, X. Li, J. W. Suk, J. R. Potts and R. S. Ruoff, *Adv. Mater.*, 2010, **22**, 3906–3924.
2 *Graphite, graphene, and their polymer nanocomposites*, ed. P. Mukhopadhyay and R. K. Gupta, CRC Press, Boca Raton, FL, 2013.

3 P. Blake, P. D. Brimicombe, R. R. Nair, T. J. Booth, D. Jiang, F. Schedin, L. A. Ponomarenko, S. V. Morozov, H. F. Gleeson, E. W. Hill, A. K. Geim and K. S. Novoselov, *Nano Lett.*, 2008, **8**, 1704–1708.
4 K. Novoselov, V. Fal, L. Colombo, P. Gellert, M. Schwab and K. Kim, *Nature*, 2012, **490**, 192–200.
5 Y. B. Tan and J. M. Lee, *J. Mater. Chem. A*, 2013, **1**, 14814–14843.
6 E. Yoo, J. Kim, E. Hosono, H. Zhou, T. Kudo and I. Honma, *Nano Lett.*, 2008, **8**, 2277–2282.
7 F. Bonaccorso, Z. Sun, T. Hasan and A. C. Ferrari, *Nat. Photonics*, 2010, **4**, 611–622.
8 L. Qu, Y. Liu, J.-B. Baek and L. Dai, *ACS Nano*, 2010, **4**, 1321–1326.
9 K. S. Kim, Y. Zhao, H. Jang, S. Y. Lee, J. M. Kim, K. S. Kim, J.-H. Ahn, P. Kim, J.-Y. Choi and B. H. Hong, *Nature*, 2009, **457**, 706–710.
10 S. Ghosh, I. Calizo, D. Teweldebrhan, E. P. Pokatilov, D. L. Nika, A. A. Balandin, W. Bao, F. Miao and C. N. Lau, *Appl. Phys. Lett.*, 2008, **92**, 151911.
11 H. Chen, M. B. Müller, K. J. Gilmore, G. G. Wallace and D. Li, *Adv. Mater.*, 2008, **20**, 3557–3561.
12 H. Kim, Y. Miura and C. W. Macosko, *Chem. Mater.*, 2010, **22**, 3441–3450.
13 J. Zhu, M. Chen, Q. He, L. Shao, S. Wei and Z. Guo, *RSC Adv.*, 2013, **3**, 22790–22824.
14 D. R. Dreyer, S. Park, C. W. Bielawski and R. S. Ruoff, *Chem. Soc. Rev.*, 2010, **39**, 228–240.
15 C. Chung, Y.-K. Kim, D. Shin, S.-R. Ryoo, B. H. Hong and D.-H. Min, *Acc. Chem. Res.*, 2013, **46**, 2211–2224.
16 G. Z. Kyzas, E. A. Deliyanni and K. A. Matis, *J. Chem. Technol. Biotechnol.*, 2014, **89**, 196–205.
17 J. Zhu, S. Wei, H. Gu, S. B. Rapole, Q. Wang, Z. Luo, N. Haldolaarachchige, D. P. Young and Z. Guo, *Environ. Sci. Technol.*, 2012, **46**, 977–985.
18 J. Zhu, M. Chen, H. Qu, X. Zhang, H. Wei, Z. Luo, H. A. Colorado, S. Wei and Z. Guo, *Polymer*, 2012, **53**, 5953–5964.
19 J. Yuan, J. Zhu, H. Bi, X. Meng, S. Liang, L. Zhang and X. Wang, *Phys. Chem. Chem. Phys.*, 2013, **15**, 12940–12945.
20 Y. Zhang, Z.-R. Tang, X. Fu and Y.-J. Xu, *ACS Nano*, 2010, **4**, 7303–7314.
21 G. Zhou, D.-W. Wang, F. Li, L. Zhang, N. Li, Z.-S. Wu, L. Wen, G. Q. Lu and H.-M. Cheng, *Chem. Mater.*, 2010, **22**, 5306–5313.
22 L. Fan, C. Luo, M. Sun and H. Qiu, *J. Mater. Chem.*, 2012, **22**, 24577–24583.
23 J. Li, S. Zhang, C. Chen, G. Zhao, X. Yang, J. Li and X. Wang, *ACS Appl. Mater. Interfaces*, 2012, **4**, 4991–5000.
24 X. Hu, Y. Liu, H. Wang, A. Chen, G. Zeng, S. Liu, Y. Guo, X. Hu, T. Li, Y. Wang, L. Zhou and S. Liu, *Sep. Purif. Technol.*, 2013, **108**, 189–195.
25 V. Chandra, J. Park, Y. Chun, J. W. Lee, I.-C. Hwang and K. S. Kim, *ACS Nano*, 2010, **4**, 3979–3986.
26 G. Gollavelli, C.-C. Chang and Y.-C. Ling, *ACS Sustainable Chem. Eng.*, 2013, **1**, 462–472.
27 J. Zhu, R. Sadu, S. Wei, D. H. Chen, N. Haldolaarachchige, Z. Luo, J. A. Gomes, D. P. Young and Z. Guo, *ECS J. Solid State Sci. Technol.*, 2012, **1**, M1–M5.
28 J.-H. Deng, X.-R. Zhang, G.-M. Zeng, J.-L. Gong, Q.-Y. Niu and J. Liang, *Chem. Eng. J.*, 2013, **226**, 189–200.
29 W. Zhang, X. Shi, Y. Zhang, W. Gu, B. Li and Y. Xian, *J. Mater. Chem. A*, 2013, **1**, 1745–1753.
30 H. Sun, L. Cao and L. Lu, *Nano Res.*, 2011, **4**, 550–562.
31 L. Ai, C. Zhang and Z. Chen, *J. Hazard. Mater.*, 2011, **192**, 1515–1524.
32 S. Bai, X. Shen, X. Zhong, Y. Liu, G. Zhu, X. Xu and K. Chen, *Carbon*, 2012, **50**, 2337–2346.
33 W. S. Hummers and R. E. Offeman, *J. Am. Chem. Soc.*, 1958, **80**, 1339.
34 M. Wang, X. Shao, W. Li, H. Li, J. Yin and F. Liu, *J. Alloys Compd.*, 2014, **596**, 1–4.
35 M. Zong, Y. Huang, Y. Zhao, X. Sun, C. Qu, D. Luo and J. Zheng, *RSC Adv.*, 2013, **3**, 23638–23648.
36 S. Park, J. An, I. Jung, R. D. Piner, S. J. An, X. Li, A. Velamakanni and R. S. Ruoff, *Nano Lett.*, 2009, **9**, 1593–1597.
37 J. I. Paredes, S. Villar-Rodil, A. Martínez-Alonso and J. M. D. Tascón, *Langmuir*, 2008, **24**, 10560–10564.
38 Y. Xue, H. Chen, D. Yu, S. Wang, M. Yardeni, Q. Dai, M. Guo, Y. Liu, F. Lu, J. Qu and L. Dai, *Chem. Commun.*, 2011, **47**, 11689–11691.
39 Y. Yao, S. Miao, S. Yu, L. Ping Ma, H. Sun and S. Wang, *J. Colloid Interface Sci.*, 2012, **379**, 20–26.
40 A. V. Murugan, T. Muraliganth and A. Manthiram, *Chem. Mater.*, 2009, **21**, 5004–5006.
41 H.-K. Jeong, H.-J. Noh, J.-Y. Kim, M. H. Jin, C. Y. Park and Y. H. Lee, *EPL*, 2008, **82**, 67004.
42 M. Acik, G. Lee, C. Mattevi, A. Pirkle, R. M. Wallace, M. Chhowalla, K. Cho and Y. Chabal, *J. Phys. Chem. C*, 2011, **115**, 19761–19781.
43 T. Szabó, O. Berkesi and I. Dékány, *Carbon*, 2005, **43**, 3186–3189.
44 M. Seredych and T. J. Bandosz, *J. Phys. Chem. C*, 2010, **114**, 14552–14560.
45 H. J. Salavagione, G. Martínez and M. A. Gómez, *J. Mater. Chem.*, 2009, **19**, 5027–5032.
46 E.-Y. Choi, T. H. Han, J. Hong, J. E. Kim, S. H. Lee, H. W. Kim and S. O. Kim, *J. Mater. Chem.*, 2010, **20**, 1907–1912.
47 M. Fu, Q. Jiao and Y. Zhao, *J. Mater. Chem. A*, 2013, **1**, 5577–5586.
48 S. Goenka, V. Sant and S. Sant, *J. Controlled Release*, 2014, **173**, 75–88.
49 H. Wang, Z. Xu, H. Yi, H. Wei, Z. Guo and X. Wang, *Nano Energy*, 2014, **7**, 86–96.
50 V. K. Singh, M. K. Patra, M. Manoth, G. S. Gowd, S. R. Vadera and N. Kumar, *New Carbon Mater.*, 2009, **24**, 147–152.
51 M. Veerapandian, M.-H. Lee, K. Krishnamoorthy and K. Yun, *Carbon*, 2012, **50**, 4228–4238.
52 K. N. Kudin, B. Ozbas, H. C. Schniepp, R. K. Prud'homme, I. A. Aksay and R. Car, *Nano Lett.*, 2008, **8**, 36–41.
53 A. C. Ferrari, *Solid State Commun.*, 2007, **143**, 47–57.

54 K. Krishnamoorthy, M. Veerapandian, R. Mohan and S.-J. Kim, *Appl. Phys. A*, 2012, **106**, 501–506.
55 N. J. Bell, Y. H. Ng, A. Du, H. Coster, S. C. Smith and R. Amal, *J. Phys. Chem. C*, 2011, **115**, 6004–6009.
56 J. Zhu, S. Wei, N. Haldolaarachchige, J. He, D. P. Young and Z. Guo, *Nanoscale*, 2012, **4**, 152–156.
57 J. Zhu, Z. Luo, S. Wu, N. Haldolaarachchige, D. P. Young, S. Wei and Z. Guo, *J. Mater. Chem.*, 2012, **22**, 835–844.
58 M. Veerapandian, Y.-T. Seo, H. Shin, K. Yun and M.-H. Lee, *Int. J. Nanomed.*, 2012, **7**, 6123–6136.
59 F. Tuinstra, *J. Chem. Phys.*, 1970, **53**, 1126–1130.
60 S. Zhu, J. Guo, J. Dong, Z. Cui, T. Lu, C. Zhu, D. Zhang and J. Ma, *Ultrason. Sonochem.*, 2013, **20**, 872–880.
61 L. G. Cançado, K. Takai, T. Enoki, M. Endo, Y. A. Kim, H. Mizusaki, A. Jorio, L. N. Coelho, R. Magalhães-Paniago and M. A. Pimenta, *Appl. Phys. Lett.*, 2006, **88**, 163106.
62 A. M. Gadalla and H.-F. Yu, *J. Mater. Res.*, 1990, **5**, 1233–1236.
63 M. Z. Kassaee, E. Motamedi and M. Majdi, *Chem. Eng. J.*, 2011, **172**, 540–549.
64 B. C. Giessen and G. E. Gordon, *Science*, 1968, **159**, 973–975.
65 G. Zhao, J. Li, X. Ren, C. Chen and X. Wang, *Environ. Sci. Technol.*, 2011, **45**, 10454–10462.
66 Q. Hao, S. Liu, X. Yin, Z. Du, M. Zhang, L. Li, Y. Wang, T. Wang and Q. Li, *CrystEngComm*, 2011, **13**, 806–812.
67 A. Taylor and H. Sinclair, *Proc. Phys. Soc., London*, 1945, **57**, 126–135.
68 J. Guo, H. Gu, H. Wei, Q. Zhang, N. Haldolaarachchige, Y. Li, D. P. Young, S. Wei and Z. Guo, *J. Phys. Chem. C*, 2013, **117**, 10191–10202.
69 H. Li, W. Li, Y. Zhang, T. Wang, B. Wang, W. Xu, L. Jiang, W. Song, C. Shu and C. Wang, *J. Mater. Chem.*, 2011, **21**, 7878–7881.
70 H.-J. Song, X.-H. Jia, H. Qi, X.-F. Yang, H. Tang and C.-Y. Min, *J. Mater. Chem.*, 2012, **22**, 3508–3516.
71 Y.-P. Sun, X.-q. Li, J. Cao, W.-x. Zhang and H. P. Wang, *Adv. Colloid Interface Sci.*, 2006, **120**, 47–56.
72 G. Sobon, J. Sotor, J. Jagiello, R. Kozinski, M. Zdrojek, M. Holdynski, P. Paletko, J. Boguslawski, L. Lipinska and K. M. Abramski, *Opt. Express*, 2012, **20**, 19463–19473.
73 L. L. Zhang, X. Zhao, M. D. Stoller, Y. Zhu, H. Ji, S. Murali, Y. Wu, S. Perales, B. Clevenger and R. S. Ruoff, *Nano Lett.*, 2012, **12**, 1806–1812.
74 H. Liu, L. Zhang, Y. Guo, C. Cheng, L. Yang, L. Jiang, G. Yu, W. Hu, Y. Liu and D. Zhu, *J. Mater. Chem. C*, 2013, **1**, 3104–3109.
75 P. Chen, K. Xu, X. Li, Y. Guo, D. Zhou, J. Zhao, X. Wu, C. Wu and Y. Xie, *Chem. Sci.*, 2014, **5**, 2251–2255.
76 J. Zhu, S. Wei, X. Chen, A. B. Karki, D. Rutman, D. P. Young and Z. Guo, *J. Phys. Chem. C*, 2010, **114**, 8844–8850.